Ultrasound in Med. & Biol., Vol. ■, No. ■, pp. 1–8, 2013

0301-5629/$ - see front matter

http://dx.doi.org/10.1016/j.ultrasmedbio.2013.10.011

● *Original Contribution*

CHARACTERIZING PHANTOM ARTERIES WITH MULTI-CHANNEL LASER ULTRASONICS AND PHOTO-ACOUSTICS

JAMI L. JOHNSON,*† KASPER VAN WIJK,† and MICHELLE SABICK*

*Mechanical and Biomedical Engineering Department, Boise State University, Boise, Idaho, USA; and †Department of Physics, University of Auckland, Auckland, New Zealand

(*Received* 24 *May* 2013; *revised* 7 *September* 2013; *in final form* 8 *October* 2013)

Abstract—Multi-channel photo-acoustic and laser ultrasonic waves are used to sense the characteristics of proxies for healthy and diseased vessels. The acquisition system is non-contacting and non-invasive with a pulsed laser source and a laser vibrometer detector. As the wave signatures of our targets are typically low in amplitude, we exploit multi-channel acquisition and processing techniques. These are commonly used in seismology to improve the signal-to-noise ratio of data. We identify vessel proxies with a diameter on the order of 1 mm, at a depth of 18 mm. Variations in scattered and photo-acoustic signatures are related to differences in vessel wall properties and content. The methods described have the potential to improve imaging and better inform interventions for atherosclerotic vessels, such as the carotid artery. (E-mail: jami.johnson@auckland.ac.nz) © **2013 World Federation for Ultrasound in Medicine & Biology.**

Key Words: **Photo-acoustic imaging, Laser ultrasound, Calcification, Ultrasound imaging, Multi-channel imaging, Atherosclerosis.**

INTRODUCTION

The relationship between atherosclerotic plaque morphology in the carotid artery and cerebrovascular events has been of interest for many years (Faggioli et al. 2011; Gomez 1990; Mendis et al. 2011; Wang 2009; Wexler et al. 1996). Compositional factors contribute to the vulnerability of an atherosclerotic plaque to rupture, as opposed to degree of stenosis or patient symptoms (Wallis de Vries et al. 2008). These factors include the presence and size of lipid pools, thickness of the fibrous cap and presence of inflammation and calcification (Fok 2012; Naghavi et al. 2003; Sethuraman et al. 2005; Virmani et al. 2000). Additionally, the geometry of an atherosclerotic vessel may contribute to rupture risk (Pasterkamp et al. 1999).

Currently, no imaging modality can unambiguously identify vulnerable atherosclerotic plaques with the needed resolution in a non-invasive manner (Wallis de Vries et al. 2008). To image arteries and identify stenosis, angiography is often used (Richards-Kortum 2010). However, angiography uses ionizing radiation, requires the injection of a radiopaque dye and is not recommended for characterizing atherosclerotic lesions (Baumgart et al. 1997). Optical methods, such as optical coherence tomography (Wang et al. 2010), Fourier transform infrared spectroscopy and Raman spectroscopy (Lattermann et al. 2013), can identify molecules with unique spectral signatures, such as lipids and hemoglobin. Resolution is on the order of 10 μm, but optical scattering limits depth penetration to about 1 mm (Lattermann et al. 2013). Multi-contrast magnetic resonance imaging can detect lipid cores and intraplaque hemorrhage in large arteries with sub-millimeter resolution (Briley-Saebo et al. 2007). High cost, low signal-to-noise ratio, motion artifact and long acquisition times limit widespread use of magnetic resonance imaging for plaque screening (Briley-Saebo et al. 2007; Richards-Kortum 2010; Saam et al. 2007).

Electron-beam computed tomography and multi-slice computed tomography are considered the gold standard for evaluating the extent and advancement of vascular calcification (Raggi and Bellasi 2007). A slice thickness as small as 0.5 to 0.75 mm can be used (Mollet et al. 2005), but high cost, significant radiation exposure and reproducibility concerns for small lesions limit CT modalities for calcification screening (Raggi and Bellasi 2007; Wexler et al. 1996). Conversely, ultrasound imaging is low cost, portable and safe (Raggi and Bellasi 2007).

Address correspondence to: Jami Johnson, Science Centre, 38 Princes Street, Auckland, New Zealand. E-mail: jami.johnson@auckland.ac.nz

Calcification is characterized by hyperechoic amplitudes and acoustic shadowing. Despite these advantages, ultrasound has low sensitivity for calcification detection, and acoustic shadowing rarely accompanies small calcifications (Taki et al. 2012). Intravascular ultrasound acquires cross-sectional images of vessels with a resolution of 0.05–0.1 mm, but is limited to depths of about 5–10 mm (Richards-Kortum 2010). The invasive nature, cost and additional operative time and equipment prohibit widespread use of intravascular ultrasound for routine plaque characterization (Arthurs et al. 2010).

Photo-acoustic (PA) waves can image artery structure and certain plaque constituents with unique spectral signatures. For example, lipids are imaged with high resolution and contrast (Allen et al. 2012). PA imaging is absorption based. The rapid absorption of modulated light causes thermo-elastic expansion and subsequent emission of acoustic waves. The depth limitations of purely optical modalities are overcome using PA methods, as multiple optical scattering events help to uniformly illuminate chromophores, and ultrasonic scattering is two to three orders of magnitude weaker than optical scattering. Therefore, PA imaging provides information about optical absorption while still allowing for high resolution deep within tissue (Wang 2009; Yao and Wang 2011).

The application of PA imaging to atherosclerotic plaque characterization is also beginning to be explored. Recently, the optical spectrum of lipids was exploited to visualize lipid pools within the wall of a human aorta using PA imaging (Allen et al. 2012). Additional advances include characterization of atherosclerotic plaques using intravascular ultrasound and PA techniques (Li et al. 2012; Sethuraman et al. 2005; Wang et al. 2012) and PA detection of the inflammatory response of atherosclerotic lesions using gold nanorods as a targeting agent (Ha et al. 2011; Kim et al. 2007; Yeager et al. 2012).

Calcification is not readily detected using PA methods, because calcium has an indistinct optical spectrum. The acoustic properties of calcification, however, are different from those of soft tissue. These properties can be exploited by generating an acoustic wave at the tissue surface and measuring the scattered wave field as in traditional ultrasound imaging. A source laser can be chosen such that a PA wave is generated in the vessel and a laser ultrasound (LU) wave is generated at the tissue surface. Observing the behavior of both PA and LU waves may provide the necessary information about plaque constituents, such as lipid pools, as well as calcification.

Rousseau et al. (2012a, 2012b) obtained dual photo-acoustic and ultrasound images using interferometric detection. High-resolution images of structures beyond 1 cm deep were obtained (300 μm), but hyperbolic artifacts remain from limitations in image reconstruction. Here, we exploit both the optical and acoustic properties of artery surrogates using multi-channel PA and LU techniques to boost the signal-to-noise ratio for weakly scattering targets. Phantom studies are presented using a laser source and a scanning vibrometer to detect the acoustic signals. We detect structures on the order of 1 mm and changes in acoustic impedance for a wall thickness less than 250 μm. Our motivation is to improve PA and LU resolution at depths beyond 1 cm using multiple detection channels for a single source position. To take full advantage of these multi-channel data, we use image processing techniques common in multi-channel seismic methods. This has the potential advantage of determination of several constituents of atherosclerotic plaque and structure geometry with high sensitivity. In vessels such as the carotid artery, the information obtained can be used to inform both preventative treatments and surgical interventions. Improved detection of calcification caused by implanted grafts, stents or valves may also reduce complications. The current tools and methods use only non-ionizing radiation and have the advantages of being hands-free, non-contact and non-invasive.

METHODS

A phantom was constructed to simulate the optical scattering and acoustic properties of human tissue. The phantom is composed of 1% Intralipid (Fresenius Kabi, Uppsala, Sweden), 1% highly purified agar (A0930-05, U.S. Biological, Swampscott, MA, USA) and distilled water. Intralipid is a phospholipid emulsion that is widely used for optical and photo-acoustic phantom studies, because it is a homogeneous and turbid medium without distinct absorption bands (Cubeddu et al. 1997; Driver et al. 1989; Flock et al. 1992; Kinnunen and Myllylä 2005; Yao et al. 2010). Agar was used to solidify the phantom, without notably increasing turbidity or optical absorption (Cubeddu et al. 1997).

Artery surrogates that mimic absorbing and scattering properties of vascular structures with varying compositions were embedded 18 mm below the surface of the phantom. A thin-walled polyester tube (inner diameter = 1.57 mm, wall thickness = 12.7 μm, Advanced Polymers, Salem, NH, USA) represents a healthy vessel. This tube is optically and acoustically clear at the wavelengths used. In contrast, an optically clear acrylic tube (inner diameter = 1.4 mm, wall thickness = 233.5 μm, Paradigm Optics, Vancouver, WA, USA) represents a calcified artery. The thicker acrylic wall has a modulus of rigidity comparable to that of a calcified artery ($\sim$1.8 GPa), and imposes an acoustic contrast in our sample (Afifi 2003). Both tubes first contained air, but we also mimic the presence of

blood in the vessels with an infrared absorbing dye (Epolight 2057, Epolin, Newark, NJ, USA) dissolved in isopropyl alcohol. A phantom-only trial was recorded for a total of five trials (Table 1).

The optical and acoustic properties of each phantom artery determine the magnitude of PA generation and LU scattering, respectively. The fraction of an acoustic wave reflected at the interface between two media is defined by the reflection coefficient

$$R = \frac{Z - Z_0}{Z + Z_0}, \quad (1)$$

where $Z = \rho v$ is the acoustic impedance of the medium: the product of density ρ and acoustic velocity v. The photo-acoustic amplitude is proportional to the optical absorption coefficient of the medium and the energy of the source beam (Beard 2011). Table 2 outlines the relevant acoustic and optical properties for each medium used, and the theoretical reflection coefficients for each interface are recorded in Table 3.

The experimental setup is illustrated in Figure 1. A 1064-nm neodymium-doped yttrium aluminum garnet (Nd:YAG) source laser was used (Quanta-Ray, Spectra Physics, Newport, Irvine, CA, USA). The beam was unfocused (diameter = 8 mm) with a 10-ns pulse width and 11-Hz repetition rate. The pulse energy was maintained at approximately 100 mJ/cm^2, but we recognize additional energy considerations are required to keep the laser exposure for human tissue below the American National Standards Institute maximum permissible exposure for repetitive pulses at 1064 nm (American National Standards Institute 2007). The source beam incident on the phantom surface provides both penetration of the laser light into the phantom for PA generation by the dye and absorption of the source at the surface for LU generation (Fig. 2). A scanning heterodyne vibrometer detects the PA and LU wave fields (PSV-400, Polytec, Irvine, CA, USA). A reflective tape was placed across the detection surface to enhance sensitivity of signal detection by the vibrometer. Line scans were recorded in reflection mode, where the detection beam was scanned by 336.9-μm increments away from the location of the source beam, with an average of 64 A-scans recorded per beam location (Fig. 1). A total of 95 wave fields were recorded, covering a total scan distance of 3.2 cm.

Table 1. Summary of experiments*

	Tube type				
	None	Polyester		Acrylic	
Trial number	1	2	3	4	5
Tube filling	—	Air	Dye	Air	Dye

* Trial numbers correspond to the type of tube embedded in the phantom and its content.

Table 2. Acoustic and optical properties of tissue phantom and embedded media*

Medium	Mass density, ρ (kg/m^3)	Speed of sound, v (m/s)	μ_a† (cm^{-1})
Phantom	1000	1390	0.15
Polyester	1400	2400	—
Acrylic	1180	2740	—
Air	1.2	343	—
Dye	786	1170	20

* From Bloomfield et al. (2000), Selfridge (1985), Pavan et al. (2010), Afifi (2003) and Beard (2011).
† μ_a = optical absorption coefficient.

RESULTS

With the exception of trial 1, each of the trials detected a phantom vessel. The B-scan for trial 5, an acrylic tube filled with dye inside the phantom, is provided in Figure 3. The arrival time, t, of the PA and LU waves scattered from the phantom vessel are a function of the receiver location, x, and the wave speed in the phantom tissue, v,

$$t^2 = t_0^2 + (x/v)^2, \quad (2)$$

where t_0 is the time associated with the waves traveling from source to scatterer. In the PA experiment, $t_0 \approx 0$, as the ultrasound is generated at the phantom vessel. In addition to the LU and PA waves from the scatterer, we detect a low-frequency wave that propagates through the air and a wave that goes directly from source to receiver through the phantom.

A high-pass Butterworth filter (100-kHz cutoff frequency) was used to remove the low-frequency air wave. The direct wave was removed using a frequency-wavenumber (f-k) filter (for further detail on the f-k filter design, see Johnson [2013]). Often called velocity filters, f-k filters are used in multi-channel (seismic) recordings to separate or remove waves arriving from different directions (Bing et al. 2011; Hayashi and Sato 2010). Figure 3 is the B-scan after the band-pass filter and the suppression of waves arriving with an apparent velocity between 1380 and 1400 m/s.

Semblance

A correction for the path-length difference for different values of the PA and LU waves as a function

Table 3. Reflection coefficient, R (eqn [1]), for the interface between the tissue phantom and each embedded medium

Interface	R
Phantom-air	~ –1
Phantom-dye	–0.2
Phantom-polyester	~0
Phantom-acrylic	0.4

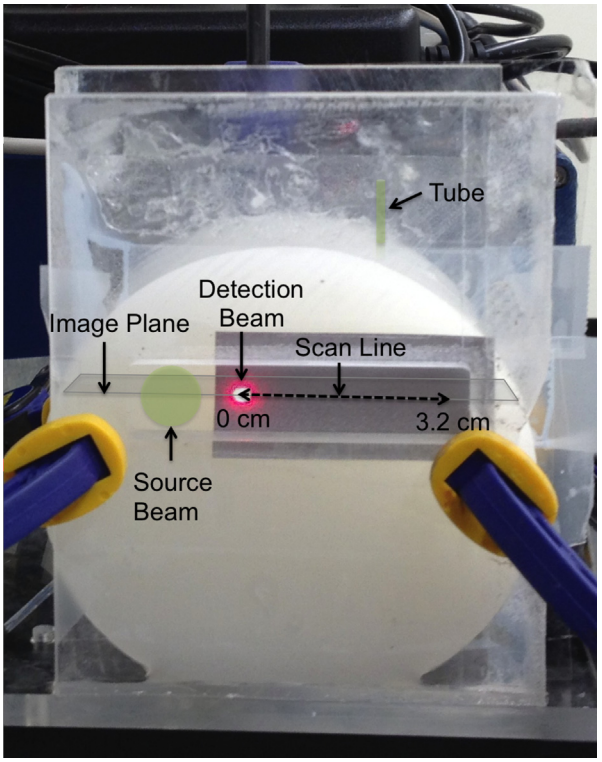

Fig. 1. Photograph of experimental setup. The vessel proxy is placed under the midway point of the receiver scan line.

of receiver location, x (eqn [2]), was made so that all waves appear to arrive at the same time, t_0. In multichannel seismic processing, this is called a normal move-out (NMO) correction (Dunkin and Levin 1973; Rupert and Chun 1975).

With the proper correction (*i.e.,* the correct value of v), the waves for all receiver positions, x, arrive at t_0. In practice, v is not (exactly) known, and we iterate the process for different values of v, until the corrected waveforms align, and the sum of the aligned waveforms has the largest amplitude. The ratio of summed amplitude of the signal to the average of the noise level is termed *semblance*:

$$S = \sqrt{\frac{\max(\text{signal}^2)}{\text{mean}(\text{noise}^2)}}. \quad (3)$$

The wave speed at maximum semblance is an accurate measure of the speed of sound in the medium, and the maximum semblance value can be used as an objective measure of resolving contrast. NMO-corrected images and corresponding stacked traces are provided for trial 5 in Figure 4 and traces for trial 2 and trial 3 in Figure 5.

Maximum semblance values, S, for each trial are listed in Table 4. For comparison, we also report the signal-to-noise ratio of the single-channel recording, where the receiver is positioned directly over the target. The details of the NMO correction and semblance analysis are described in Johnson (2013).

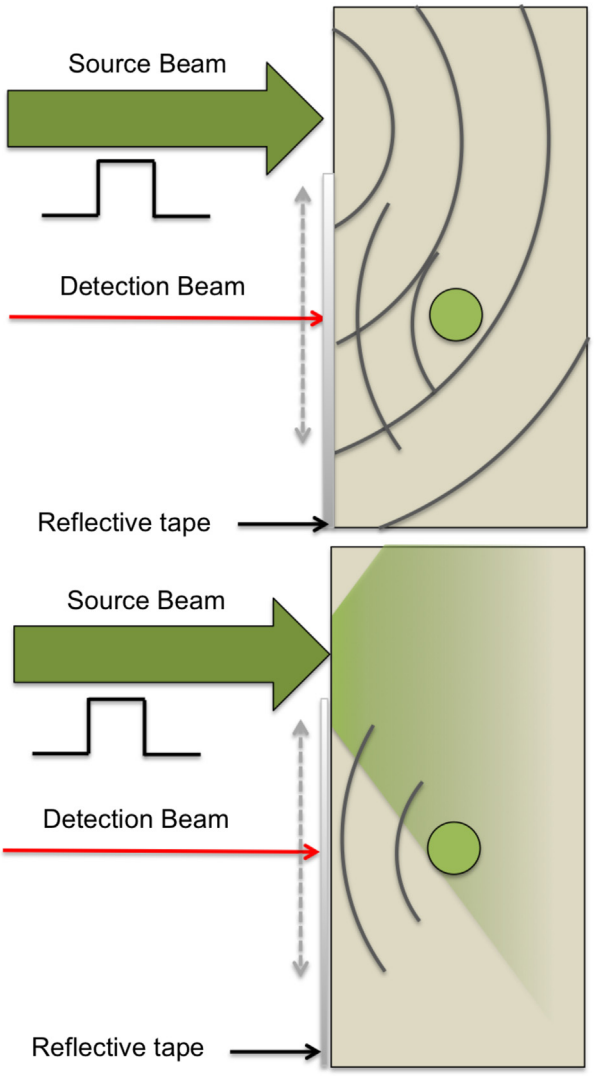

Fig. 2. Diagrams of laser ultrasound (*top*) and photo-acoustic (*bottom*) generation and scattering in the transverse plane of the phantom. In the bottom panel, the optical energy of the source beam is shown illuminating an absorber embedded in the phantom, which generates a photo-acoustic wave. A laser ultrasound wave generated at the surface of the phantom is shown in the top panel. The laser ultrasound and photo-acoustic waves are detected at the phantom surface.

DISCUSSION

All LU and PA trials detected the phantom vessel. Here, we briefly discuss some of the observations for each trial.

Because the outer diameters of the two tubes are comparable, the thinner-walled tube has a larger internal volume. With air in the tubes, LU scattering in trial

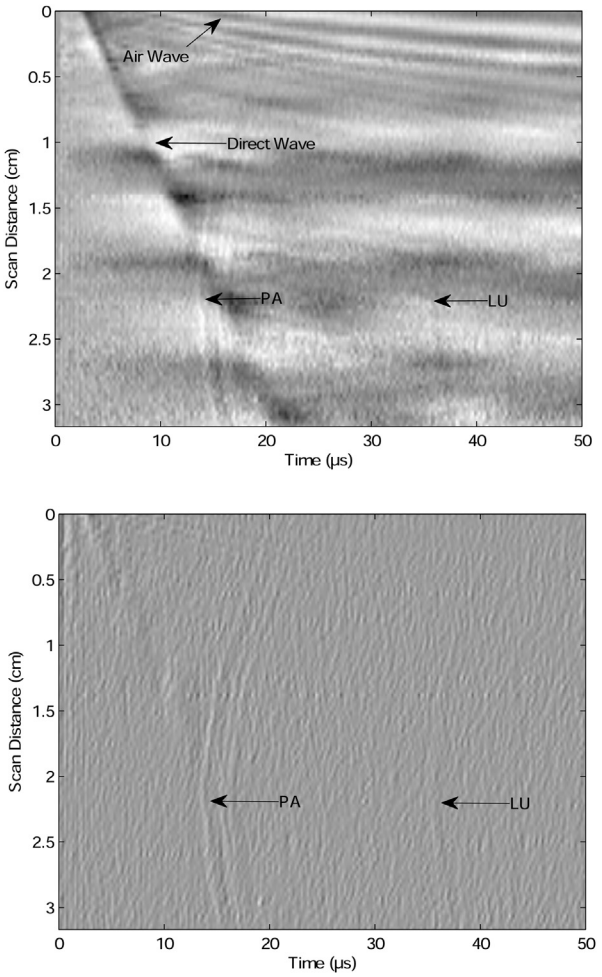

Fig. 3. B-Scan of trial 5 (acrylic tube filled with dye) before (*top*) and after (*bottom*) band-pass and frequency-wavenumber filtering.

2 (thin) is stronger than that in trial 4 (thicker tube). We attribute this to the larger elastic impedance contrast between air and the tissue phantom material. With dye in the tubes, the impedance contrast with the tissue phantom is apparently dominated by the tube walls: the thicker-walled tube has stronger LU scattering.

Dye inside the tubes in trials 3 and 5, representing hemoglobin, resulted in stronger PA generation than with air. On the basis of the maximum semblance for each trial stated in Table 4, the amplitude of the PA wave generated in the thinner polyester tube was significantly higher than that of the wave generated in the thicker acrylic tube. Although a slight hyperechoic effect was expected by PA generation in a stiff tube, it appears that the relatively larger volume of dye in the thinner

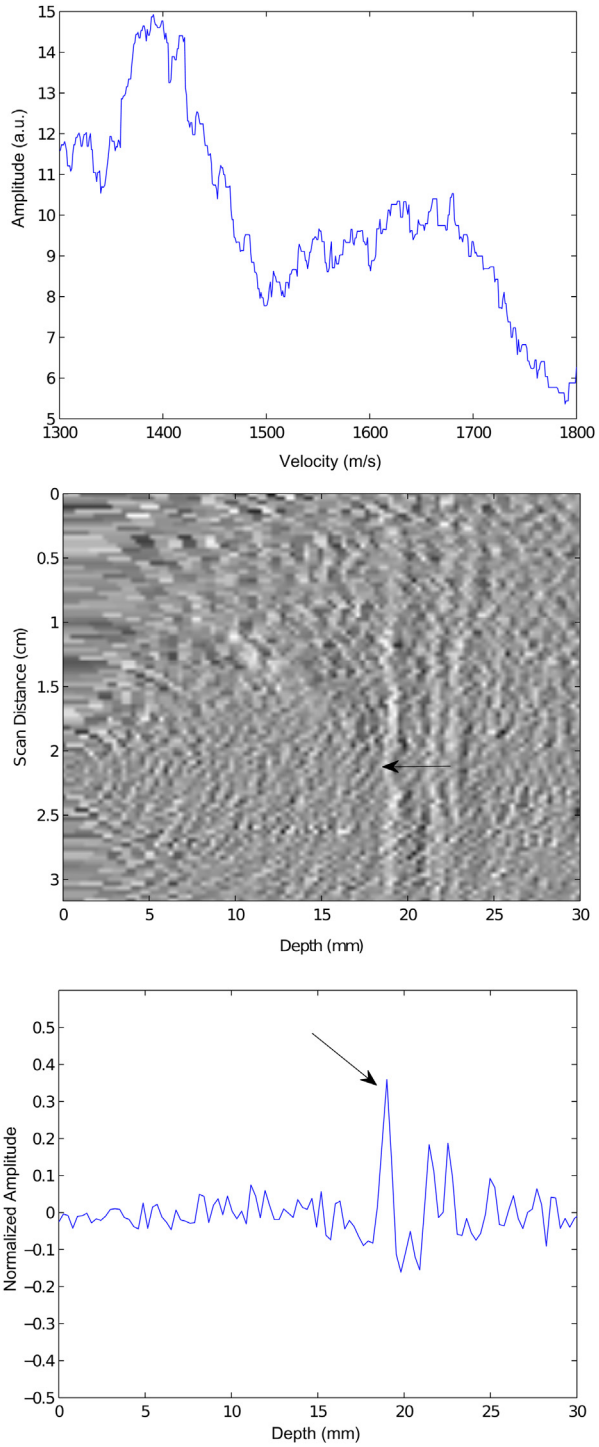

Fig. 4. (*Top*) Semblance of the photo-acoustic (PA) wave for the acrylic tube filled with dye (trial 5), as a function of velocity (optimum value $v = 1390$ m/s). (*Middle*) Normal move-out (NMO)-corrected waveforms. (*Bottom*) Stack (sum) of NMO-corrected waveforms. An arrow points to the location of the scatterer. Evidence of the generated PA wave resonating follows the first arrival (see Johnson 2013).

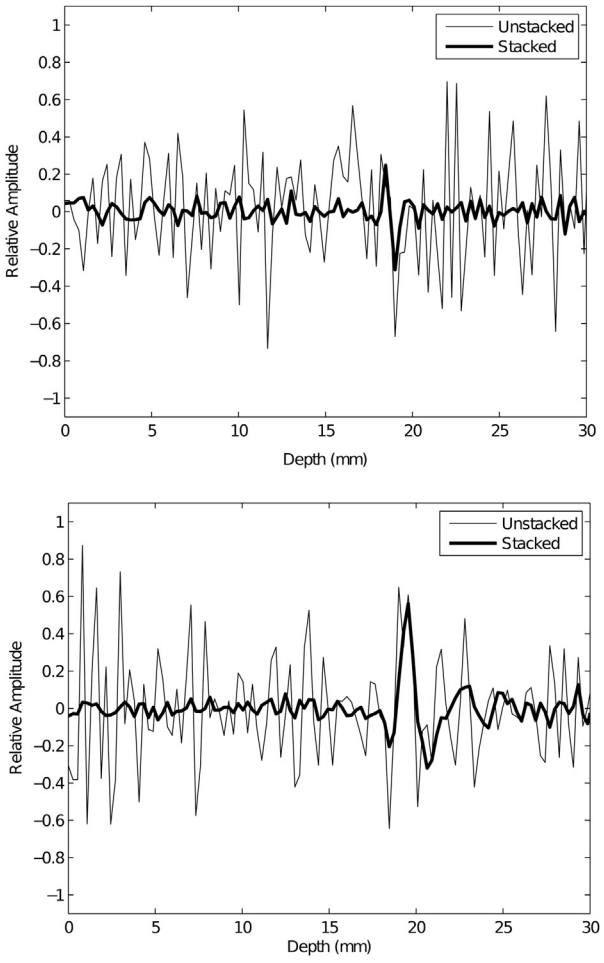

Fig. 5. Waveforms for trial 2 (*top*) and trial 3 (*bottom*) before and after the semblance analysis and stacking of the photo-acoustic and laser ultrasound waves. The unstacked traces were recorded directly above the scatterer.

tube of trial 3 results in more absorption and a higher PA wave amplitude than in trial 5.

Trial 5 with its thicker wall size and dye generated stronger LU scattering and weaker PA generation than trial 3. In general, stronger LU scattering and weaker PA generation may be an indication of an effective increase in vessel wall thickness, potentially related to calcification. We found that the LU signals were of a higher frequency than the PA waves: ~1 MHz versus ~500 kHz, respectively. The PA generating tube has a diameter of about 1.5 mm, corresponding to an expected frequency f_{PA} = (1390 m/s)/(2 × 1.5 mm) ≈ 460 kHz, which is in good agreement with our experimental data. It appears that the PA wavelength is dominated by resonant modes defined by the size of the vessel. This notion is further confirmed by reverberations observed in Figure 4.

Table 4. Maximum semblance, *S*, for each trial*

	Trial 1	Trial 2	Trial 3	Trial 4	Trial 5
PA					
NMO stack	n/a	n/a	18	n/a	13
Unstacked	n/a	n/a	—	n/a	—
LU					
NMO stack	n/a	6.9	—	3.6	5.1
Unstacked	n/a	—	—	—	—

* Large values correspond to a higher ratio of signal wave amplitude to background noise level.

Recording multiple receiver positions for each source position proved advantageous. First, it allows us to apply spatial frequency filtering (Fig. 3). Second, the frequency of LU excitation is angle dependent. In fact, pressure wave generation is at a minimum in the direction orthogonal to the generation surface (Scruby and Drain 1990). Because the depth of the target is unknown *a priori*, it is preferable to record multiple source-receiver offsets. Stacking multi-channel recordings after a normal move-out correction greatly enhanced the signal-to-noise ratio (see Table 4 and Figs. 4 and 5). However, recording multiple receiver locations for a source position significantly increases acquisition times.

In this study, phantom arteries were chosen to simulate healthy and calcified vessels. The tube representing a calcified artery was chosen such that there was a large acoustic impedance mismatch between the tissue phantom and the tube, analogous to calcification and soft tissue. Acrylic was chosen, because it has relatively high acoustic impedance and is optically transparent at the source wavelength to ensure minimal interference with PA absorption. However, true calcification has higher impedance. When the acoustic velocity of calcification (~2000 m/s [Duck 1990]) and the density of the primary component of calcification, hydroxyapatite (~3.0 g/cm^3 [Broz et al. 1995]), are used, a rough estimate for the acoustic impedance is ~6 N·s/cm^3. Acrylic has an acoustic velocity of ~2700 m/s and density of ~1.2 g/cm^3 (Afifi 2003), resulting in an impedance of 3.2 N·s/cm^3. Therefore, we expect further improvements in detection sensitivity for calcifications of the same dimension as our tube *ex vivo*. Future work will validate this method in arteries *ex vivo*.

CONCLUSIONS

Multi-channel recordings and seismic data processing techniques enhance photo-acoustic and laser ultrasonic signals from proxies of vascular structures in phantom tissue material. Experiments were conducted with inclusions analogous to healthy and calcified arteries embedded. Using these geophysical image processing techniques, we were able to comparatively analyze relatively weak signals from photo-acoustic and laser

ultrasonic contrasts from ∼1-mm objects at a depth of ∼2 cm. The non-invasive system has potential to improve detection of both scatterers with low levels of blocking (such as calcification) and weakly absorbing chromophores. This may be particularly beneficial for determining the morphology of atherosclerotic plaque in the carotid artery.

Acknowledgments—This project was supported by National Science Foundation-Major Research Instrumentation Program Award 229722.

REFERENCES

Afifi HA. Ultrasonic pulse echo studies of the physical properties of PMMA, PS, and PVC. Polym Plast Technol 2003;42:193–205.

Allen TJ, Hall A, Dhillon AP, Owen JS, Beard PC. Spectroscopic photoacoustic imaging of lipid-rich plaques in the human aorta in the 740 to 1400 nm wavelength range. J Biomed Opt 2012;17:061209.

American National Standards Institute (ANSI). American national standard for safe use of lasers. ANSI 136.1–2007. Orlando, FL: Laser Institute of America, 2007.

Arthurs ZM, Bishop PD, Feiten LE, Eagleton MJ, Clair DG, Kashyap VS. Evaluation of peripheral atherosclerosis: A comparative analysis of angiography and intravascular ultrasound imaging. J Vasc Surg 2010;51:933–938.

Baumgart D, Schmermund A, Goerge G, Haude M, Ge J, Adamzik M, Sehnert C, Altmaier K, Groenemeyer D, Seibel R, Erbel R. Comparison of electron beam computed tomography with intracoronary ultrasound and coronary angiography for detection of coronary atherosclerosis. J Am Coll Cardiol 1997;30:57–64.

Beard J. Biomedical photoacoustic imaging. Interface Focus 2011;1:602–631.

Bing W, Guo T, Hua W, Bolei T. Extracting near-borehole P and S reflections from array sonic logging data. J Geophys Eng 2011;8:308–315.

Bloomfield PE, Lo WJ, Lewin PA. Experimental study of the acoustical properties of polymers utilized to construct PVDF ultrasonic transducers and the acousto-electric properties of PVDF and P(VDF/TRFE) films. IEEE Trans Ultrason Ferroelectr Freq Control 2000;47:1397–1404.

Briley-Saebo KC, Mulder WJM, Mani V, Hyafil F, Amirbekian V, Aguinaldo JGS, Fisher EA, Fayad ZA. Magnetic resonance imaging of vulnerable atherosclerotic plaques: Current imaging strategies and molecular imaging probes. J Magn Reson Imaging 2007;26:460–479.

Broz JJ, Simske SJ, Greenberg AR. Material and compositional properties of selectively demineralized cortical bone. J Biomech 1995;28:1357–1368.

Cubeddu R, Pifferi A, Taroni P, Torricelli A, Valentini G. A solid tissue phantom for photon migration studies. Phys Med Biol 1997;42:1971–1979.

Driver I, Feather JW, King PR, Dawson JB. The optical properties of aqueous suspensions of intralipid, a fat emulsion. Phys Med Biol 1989;34:1927–1930.

Duck FA. Physical properties of tissue: A comprehensive reference network. New York: Academic Press; 1990.

Dunkin JW, Levin FK. Effect of normal moveout on a seismic pulse. Geophysics 1973;38:635–642.

Faggioli GL, Pini R, Mauro R, Pasquinelli G, Fittipaldi S, Freyrie A, Serra C, Stella A. Identification of carotid 'vulnerable plaque' by contrast-enhanced ultrasonography: Correlation with plaque histology, symptoms and cerebral computed tomography. Eur J Vasc Endovasc Surg 2011;41:238–248.

Flock ST, Jacques SL, Wilson BC, Star WM, van Gemert MJC. Optical properties of intralipid: A phantom medium for light propagation studies. Lasers Surg Med 1992;12:510–519.

Fok PW. Growth of necrotic cores in atherosclerotic plaque. Math Med Biol 2012;29:301–327.

Gomez CR. Carotid plaque morphology and risk for stroke. Stroke 1990;21:148–151.

Ha S, Carson A, Agarwal A, Kotov NA, Kim K. Detection and monitoring of the multiple inflammatory responses by photoacoustic and molecular imaging using selectively targeted gold nanorods. Biomed Opt Express 2011;2:645–657.

Hayashi N, Sato M. F-k filter designs to suppress direct waves for bistatic ground penetrating radar. IEEE Trans Geosci Remote Sensing 2010;48:1433–1444.

Johnson JL. Toward characterization of diseased vascular structures using noncontact photoacoustic and laser-ultrasound imaging: A phantom study. Master's thesis, Boise State University, 2013.

Kim K, Huang SW, Ashkenazi S, O'Donnell M, Agarwal A, Kotov NA, Denny MF, Kaplan MJ. Photoacoustic imaging of early inflammatory response using gold nanorods. Appl Phys Lett 2007;90:223901.

Kinnunen M, Myllylä R. Effect of glucose on photoacoustic signals at the wavelengths of 1064 nm and 532 nm in pig blood and intralipid. J Phys D 2005;38:2654–2661.

Lattermann A, Matthäus C, Bergner N, Beleites C, Romeike BF, Krafft C, Brehm BR, Popp J. Characterization of atherosclerotic plaque depositions by Raman and FTIR imaging. J Biophotonics 2013;6:110–121.

Li X, Wei W, Zhou Q, Shung KK, Chen Z. Intravascular photoacoustic imaging at 35 to 80 MHz. J Biomed Opt 2012;17:106005.

Mendis S, Puska P, Norrving B, (eds). Global atlas on cardiovascular disease prevention and control. Geneva: World Health Organization; 2011.

Mollet NR, Cademartiri F, de Feyter PJ. Non-invasive multislice CT coronary imaging. Heart 2005;91:401–407.

Naghavi M, Libby P, Falk E, Casscells SW, Litovsky S, Rumberger J, Badimon JJ, Stefanadis C, Moreno P, Pasterkamp G, Fayad Z, Stone PH, Waxman S, Raggi P, Madjid M, Zarrabi A, Burke A, Yuan C, Fitzgerald PJ, Siscovick DS, Korte CLD, Aikawa M, Airaksinen KEJ, Assmann G, Becker CR, Chesebro JH, Farb A, Galis ZS, Jackson C, Jang IK, Koenig W, Lodder RA, March K, Demirovic J, Navab M, Priori SG, Rekhter MD, Bahr R, Grundy SM, Mehran R, Colombo A, Boerwinkle E, Ballantyne C, . Insull W Jr, Schwartz RS, Vogel R, Serruys PW, Hansson GK, Faxon DP, Kaul S, Drexler H, Greenland P, Muller JE, Virmani R, Ridker PM, Zipes DP, Shah PK, Willerson JT. From vulnerable plaque to vulnerable patient: A call for new definitions and risk assessment strategies: Part I. Circulation 2003;108:1664–1672.

Pasterkamp G, Schoneveld AH, van der Wal AC, Hijnen DJ, van Wolveren WJA, Plomp S, Teepen HLJM, Borst C. Inflammation of the atherosclerotic cap and shoulder of the plaque is a common and locally observed feature in unruptured plaques of femoral and coronary arteries. Arterioscler Thromb Vasc Biol 1999;19:54–59.

Pavan TZ, Madsen EL, Frank GR, Corneiro AAO, Hall TJ. Nonlinear elastic behavior of phantom materials for elastography. Phys Med Biol 2010;55:2679–2962.

Raggi P, Bellasi A. Clinical assessment of vascular calcification. Adv Chronic Kidney Dis 2007;14:37–43.

Richards-Kortum R. Biomedical engineering for global health. London: Cambridge University Press; 2010.

Rousseau G, Blouin A, Monchalin J. Non-contact photoacoustic tomography and ultrasonography for tissue imaging. Biomed Opt Express 2012a;3:16–25.

Rousseau G, Gauthier B, Blouin A, Monchalin J. Non-contact biomedical photoacoustic and ultrasound imaging. J Biomed Opt 2012b;17:061217.

Rupert GB, Chun JH. The block move sum normal moveout correction. Geophysics 1975;40:17–24.

Saam T, Hatsukami TS, Takaya N, Chu B, Underhill H, Kerwin WS, Cai J, Ferguson MS, Yuan C. Noninvasive MR imaging for characterization and assessment. Radiology 2007;244:64–77.

Scruby CB, Drain LE. Laser ultrasonics: Techniques and applications. London: Taylor & Francis; 1990.

Selfridge AR. Approximate material properties in isotropic materials. IEEE Trans Son Ultrason 1985;32:381–394.

Sethuraman S, Aglyamov S, Amirian J, Smalling R, Emelianov S. Intravascular photoacoustic imaging to detect and differentiate atherosclerotic plaques. In: Proceedings, 2005 IEEE Ultrasonics

Symposium, Rotterdam, The Netherlands, 18–21 September. New York: IEEE, 2005;1:133–136.

Taki H, Sakamoto T, Yamakawa M, Shiina T, Sato T. Small calcification indicator in ultrasonography using correlation of echoes with a modified wiener filter. J Med Ultrason 2012;39:127–135.

Virmani R, Kolodgie FD, Burke AP, Farb A, Schwartz SM. Lessons from sudden coronary death: A comprehensive morphological classification scheme for atherosclerotic lesions. Arterioscler Thromb Vasc Biol 2000;20:1262–1275.

Wallis de Vries BM, van Dam GM, Tio RA, Hillebrands JL, Slart RH, Zeebregts CJ. Current imaging modalities to visualize vulnerability within the atherosclerotic carotid plaque. J Vasc Surg 2008;48: 1620–1629.

Wang B, Karpiouk A, Yeager D, Amirian J, Litovsky S, Smalling R, Emelianov S. *In vivo* intravascular ultrasound-guided photoacoustic imaging of lipid in plaques using an animal model of atherosclerosis. Ultrasound Med Biol 2012;38:2098–2103.

Wang L, (ed). Photoacoustic imaging and spectroscopy. Boca Raton, FL: CRC Press; 2009.

Wang Z, Kyono H, Bezerra HG, Wang H, Gargesha M, Alraies C, Xu C, Schmitt JM, Wilson DL, Costa MA, Rollins AM. Semiautomatic segmentation and quantification of calcified plaques in intracoronary optical coherence tomography images. J Biomed Opt 2010;15: 061711.

Wexler L, Brundage B, Crouse J, Detrano R, Fuster V, Maddahi J, Rumberger J, Stanford W, White R, Taubert K. Coronary artery calcification: Pathophysiology, epidemiology, imaging methods, and clinical implications. Circulation 1996; 94:1175–1192.

Yao J, Wang LV. Photoacoustic tomography: Fundamental advances and prospects. Contrast Media Mol Imaging 2011;6:332–345.

Yao L, Sun Y, Jiang H. Transport-based quantitative photoacoustic tomography: simulations and experiments. Phys Med Biol 2010;55: 1917–1934.

Yeager D, Karpiouk A, Wang B, Amirian J, Sokolov K, Smalling R, Emelianov S. Intravascular photoacoustic imaging of exogenously labeled atherosclerotic plaque through luminal blood. J Biomed Opt 2012;17:106016.